JVST A
Journal of Vacuum Science & Technology A

ARTICLE

pubs.aip.org/avs/jva

Study of the structure, structural transition, interface model, and magnetic moments of CrN grown on MgO(001) by molecular beam epitaxy

Cite as: J. Vac. Sci. Technol. A 41, 053411 (2023); doi: 10.1116/6.0002546
Submitted: 2 February 2023 · Accepted: 13 July 2023 ·
Published Online: 3 August 2023

Khan Alam,[1,2] Rodrigo Ponce-Pérez,[3,4] Kai Sun,[5] Andrew Foley,[3] Noboru Takeuchi,[3,4] and Arthur R. Smith[3,a)]

AFFILIATIONS

[1]Department of Physics, King Fahd University of Petroleum and Minerals, Dhahran 31261, Saudi Arabia
[2]Interdisciplinary Research Center for Renewable Energy and Power Systems, King Fahd University of Petroleum and Minerals, Dhahran 31261, Saudi Arabia
[3]Department of Physics and Astronomy, Nanoscale and Quantum Phenomena Institute, Ohio University, Athens, Ohio 45701
[4]Centro de Nanociencias y Nanotecnología, Universidad Nacional Autónoma de México, Ensenada Baja California 22800, Mexico
[5]Department of Materials Science and Engineering, University of Michigan, Ann Arbor, Michigan 48109

[a)]**Author to whom correspondence should be addressed:** smitha2@ohio.edu

ABSTRACT

Structural phase transition is studied in high quality CrN thin films grown by molecular beam epitaxy on MgO(001) substrates. Cross-sectional transmission electron microscopy and x-ray diffraction reveal that the epitaxial relationship between CrN film and MgO substrate is $[100]_{CrN}/[100]_{MgO}$, $[110]_{CrN}/[110]_{MgO}$, and $[001]_{CrN}/[001]_{MgO}$. The films show tensile strain/compression at the CrN/MgO(001) interface, which relaxes gradually with the film growth. Temperature dependent x-ray diffraction measurements show a first-order structural phase transition. In addition to the experimental measurements, first-principles theoretical calculations have been carried out for finding a stable model for the CrN/MgO interface. These calculations determine two possible models for the interface, where a monolayer of chromium oxide is formed between the CrN and MgO layers.

I. INTRODUCTION

Chromium nitride (CrN) is getting much attention in recent years due to its electronic and magnetic properties and its potential use for cutting edge technological applications such as anticorrosive electrodes for supercapacitors,[1,2] cryogenic sensors for high magnetic fields,[3–5] high temperature thermoelectrics,[6,7] and spintronics.[8,9]

Bulk CrN has been well studied and its structural, electronic, and magnetic properties have been mostly determined.[10–12] For example, bulk CrN has a rock salt crystal structure with paramagnetic (PM) phase at room temperature (RT), but undergoes a transition to an orthorhombic crystal structure with antiferromagnetic (aFM) phase below its Néel temperature ($T_N \sim 270$–285 K).[10,11,13] Magnetic stresses have been proposed as the key cause of the structural phase transition.[11] However, in the published literature, it is difficult to reconcile disagreement about the electronic, magnetic, and structural properties of CrN thin films below its Néel temperature. In the published reports, CrN thin films have been grown by a variety of growth techniques such as molecular beam epitaxy (MBE) and radio frequency/direct current sputtering system with different Cr/N stoichiometric ratios on different kinds of substrates such as glass, sapphire, MgO, and Si. Some groups reported structural, electronic, and magnetic transitions and other groups did not observe these transitions.[14–23] In our previous studies, CrN grown by MBE on MgO(001) substrates show the magnetic transition from PM in cubic phase at RT to aFM at low temperatures.[14,20,22] At low temperatures, our magnetic results are in agreement with the orthorhombic crystal structure. However, our reflection high energy electron diffraction (RHEED) experiment determines the tetragonal/cubic crystal structure at the surface. Our calculations show that the orthorhombic crystal structure is more stable

compared to the tetragonal crystal, but the energy difference is so small that epitaxial constraints due to the substrate could offset it.[14] Our recent experiment on CrN thin films grown on glass and Si (001) substrates by radio frequency sputtering system shows an electronic transition from semiconductor at room temperature to either a metallic or semiconductor phase depending on the oxygen concentration in the films.[23]

In this paper, a detailed study has been carried out to investigate a structural phase transition observed in CrN films grown on MgO(001) substrates by MBE. RHEED, cross-sectional transmission electron microscopy (TEM), and x-ray diffraction (XRD) have been used to understand the epitaxial relationship between the CrN film and the MgO substrate. Temperature dependent x-ray diffraction measurements have been employed in the temperature range from 203 to 293 K for studying the structural phase transition in the films. First-principles theoretical calculations have been used to find a stable model for the CrN and MgO interfaces.

II. EXPERIMENTAL AND THEORETICAL METHODS

High quality CrN thin films were grown on MgO(001) substrates using a custom designed ultrahigh vacuum MBE.[24] The MgO(001) substrates were cleaned with acetone and isopropyl alcohol before loading them into a high vacuum loadlock. The substrates were further cleaned in vacuum on the growth stage by heating them to 1000 $\pm$ 30 °C under a nitrogen plasma flux until obtaining a streaky RHEED pattern. CrN film growth was commenced at 650 $\pm$ 30 °C under nitrogen rich conditions with N flux being 3.9 times more than the Cr flux. The Cr flux was generated by sublimating Cr shots in a dedicated Knudsen effusion cell. A well calibrated nitrogen flux[25] was obtained from a radio frequency N-plasma generator, which uses 99.999% ultrahigh pure nitrogen gas source. The growth process was monitored with RHEED and growth parameters were actively tuned accordingly for high quality growth. Two films studied in this paper are S45 and S73, which are 670 and 150 nm thick, respectively.

In situ RHEED was used for determining *in-plane* film quality and measuring epitaxial relation between the MgO and CrN layers. The electrons in the RHEED beam were accelerated with 20 keV energy and the RHEED beam was probing the surface at a grazing incident angle. Bragg measurement of crystal quality and determining the *out-of-plane* lattice constant of the film were carried out by XRD, which is equipped with a Cu x-ray source that emits k_α (1.5406 Å) x-ray photons. Cross-sectional transmission electron microscopy was employed for acquiring atomically resolved images of the CrN/MgO interface. Samples for the TEM measurement were prepared by *in situ* focused ion beam (FIB) lift-out methods using an FEI Helios 650 SEM/FIB, and for the surface protection from the ions, a carbon and Pt/C layers were deposited. The TEM uses a JEOL JEM-2100F field emission gun microscope with a CEOS probe corrector in scanning transmission electron microscopy mode, in which electrons are accelerated with 200 keV energy. Both high-angle annular dark-field (HAADF) and bright-field images were taken simultaneously.

The structural phase transition was studied *ex situ* by a custom designed variable temperature x-ray diffraction (VT-XRD) setup. In the VT-XRD experiment, nitrogen vapor was used to cool down the sample. X-ray spectra of the 002 peak of MgO and CrN were continuously recorded as the sample was either cooling down or warming up. The CrN temperature is determined by using the lattice constant and thermal expansion coefficient of MgO in the equation of linear thermal expansion.

Thermodynamic, structural, electronic, and magnetic properties of the CrN/MgO(001) interface have been investigated by spin-polarized first-principles total-energy calculations. Calculations were performed within the periodic Density Functional Theory (DFT) framework as implemented in the Vienna *Ab initio* Simulation Package (VASP).[26] Exchange-correlation energies are treated according to the Local Density Approximation (LDA) with the Ceperley–Alder parametrization.[27] The one-electron states are expanded using the projector-augmented wave basis (PAW)[28,29] with an energy cutoff of 460 eV. Since Cr and Mg have d-orbitals, the Hubbard correction (LDA+U)[30] is employed to treat the highly correlated electrons. The U values of 3.8 and 5.5 eV have been used for Cr and Mg atoms, respectively, similar to the previous reports.[31,32] The supercell method is employed to investigate the interface. Each supercell has a 1×1 periodicity and it contains a slab and a large vacuum space of 15 Å in order to avoid interactions between adjacent slabs. The slab is formed by seven atomic layers of MgO and eight monolayers of CrN, where the bottom layers of the MgO are frozen in their ideal positions to simulate the bulk-like environment. In the geometry optimization, we require that all force components must be less than 0.01 eV/Å, and the energy differences less than 1×10^{-4} eV. The Brillouin zone is sampled with a gamma centered k-points grid of $7 \times 7 \times 1$ employing the Monkhorst–Pack scheme.[33]

III. RESULTS AND DISCUSSION

Characteristic RHEED patterns of the (001) surface of the CrN thin film along [100], [110], [$\underline{1}$20], and [130] are shown in Fig. 1(a). The images are recorded at room temperature after finishing the growth of the film. All images show sharp and continuous streaks in the zeroth-order Laue rings that indicate high quality crystalline growth. In each RHEED pattern, unique streaks/spots are marked with Miller indices. Along [110] and [100], only zeroth-order Laue rings appear ($Z_{[110]}$ and $Z_{[100]}$); along [$\underline{1}$20], zeroth ($Z_{[\underline{1}20]}$), first ($F_{[\underline{1}20]}$), and second-order Laue rings ($S_{[\underline{1}20]}$) appear; and along [130], zeroth ($Z_{[130]}$) and second ($S_{[130]}$) order Laue rings appear. (Note: The first-order Laue ring along [130] appears below the magneto-structural transition of CrN.) The streaks in the zeroth-order Laue ring appear longer compared to the streaks in the higher order Laue rings due to the intersection of the reciprocal lattice rods with Ewald's sphere. Due to the reciprocal lattice mapping, the spacing between the streaks is inversely proportional to the interplanar spacing of the real crystal; the closer streaks represent larger interplanar spacing. The four crystallographic directions can be identified by their characteristic streak spacings. For example, the streak spacing between (00) and (1$\underline{1}$) along [110] is smaller than the spacing between two adjacent streaks along [100], [$\underline{1}$20], and [130] by $\sqrt{2}$, $\sqrt{10}$, and $\sqrt{5}$ times, respectively. The occurrence of the Laue rings along different directions and the characteristic spacing between the streaks of each ring is related to the cubic symmetry of CrN at room temperature. The streak spacing corresponds to an *in-plane* lattice constant ($a_{\parallel}$) of

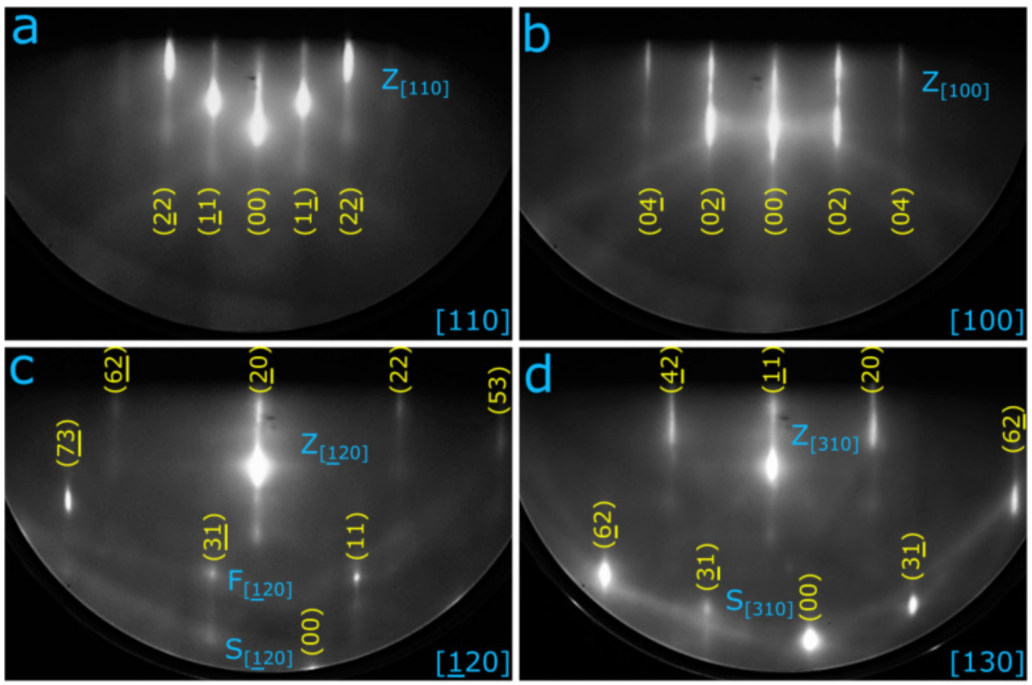

FIG. 1. RHEED patterns recorded along (a) [110], (b) [100], (c) [$\bar{1}$20], and (d) [130]. Laue rings along each direction are marked and streaks are labeled with Miller indices.

4.14 Å, which is in the range of the reported values in the literature.[16,21]

The XRD pattern of sample S45 is shown in Fig. 2. The x-ray beam consists of three wavelengths $k_\beta = 1.3923$ Å, $k_{\alpha1} = 1.540\,59$ Å, and $k_{\alpha2} = 1.544\,39$ Å. The wavelength of $k_{\alpha1}$ and $k_{\alpha2}$ is very close and cannot be filtered out completely one wavelength from another by monochromators in commercially available XRD setups; however, the intensity of $k_{\alpha1}$ is more than the intensity of $k_{\alpha2}$. At small 2θ values (approximately less than 60°), the peak produced by $k_{\alpha2}$ is convoluted and appears as a shoulder on the right side of the peaks produced by the $k_{\alpha1}$ wavelength, but at higher 2θ values the $k_{\alpha1}$ and $k_{\alpha2}$ produce separate peaks. The difference between $k_{\alpha1}$ and k_β wavelength is relatively large, but the monochromators do not filter out k_β completely from the x-ray beam. For small intensity peaks, the peak produced by k_β is negligibly small, but for high intensity peaks such as 002 peaks of MgO and CrN, the peak produced by k_β wavelength has significant intensity. The MgO peaks with the wavelength and 2θ values enclosed in parenthesis are 002 (k_β, 38.59°), 002 ($k_{\alpha1}$, 42.90°), 004 ($k_{\alpha1}$, 94.11°), and 004 ($k_{\alpha2}$, 94.40°) and CrN peaks are 002 (k_β, 39.19°), 002 ($k_{\alpha1}$, 43.54°), and 004 ($k_{\alpha1}$, 95.92°). Further detailed discussion has been provided in the supplementary material.[34] The MgO lattice constant is determined to be 4.213 Å, which is in agreement with the reported values of 4.21 Å in the literature.[35] The 002 peak of CrN appears at $2\theta = 43.54°$. The peak location corresponds to *out-of-plane* lattice constant $a_\perp = 4.152$ Å, which is in the range of the reported values of 4.13–4.17 Å.[16,21,36,37] The lattice constants of the CrN and MgO in the sample are 4.213 and 4.152 Å, respectively. These lattice constants indicate a lattice mismatch $\left(\frac{a_{CrN}-a_{MgO}}{a_{MgO}} \times 100\right)$ of 1.45%.

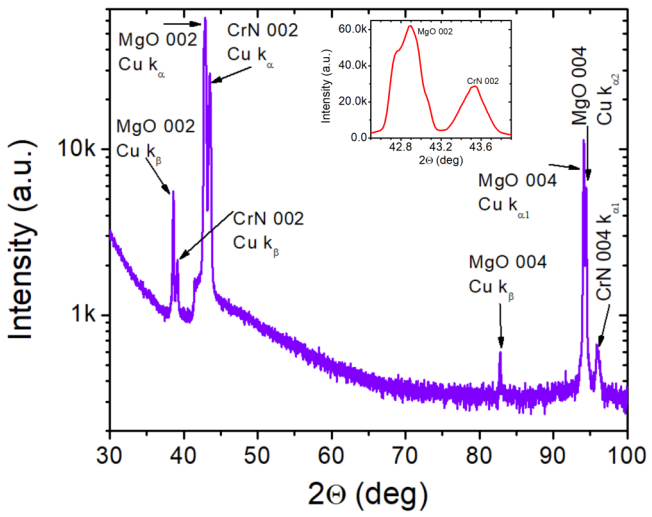

FIG. 2. X-ray diffraction pattern of sample S45. The inset shows a zoomed-in view of the 002 peaks of MgO and CrN.

Shown in Fig. 3(a) is a cross-sectional HAADF image of CrN/MgO(001) interface of S73 thin film at low magnification. The

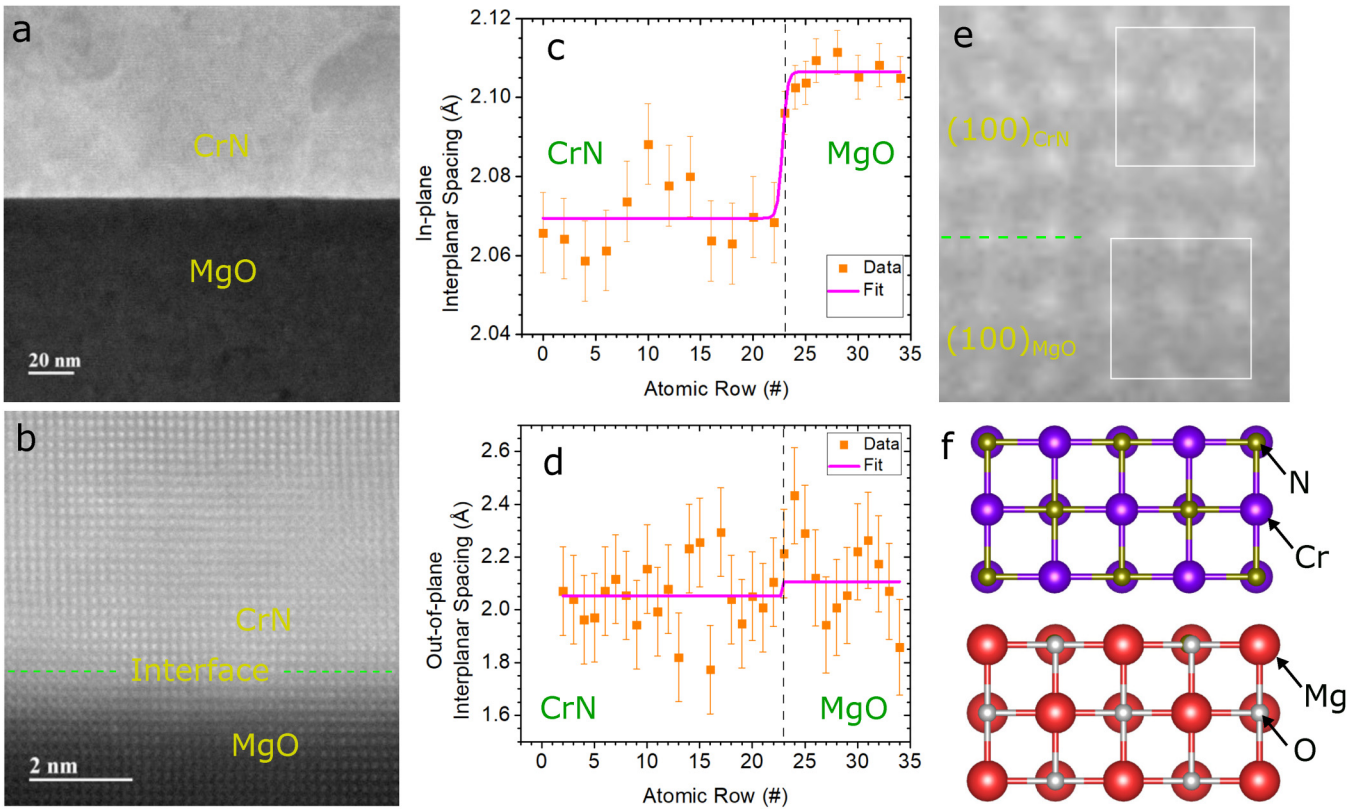

FIG. 3. (a) STEM image of CrN/MgO(001) bilayer thin films. (b) Atomically resolved image of the CrN/MgO interface. (c) *In-plane* and (d) *out-of-plane* interplanar spacing versus the number of layers with respect to the interface. (e) Atomically resolved STEM image of the interface showing $(100)_{CrN}$ and $(100)_{MgO}$ lattice planes and (f) related model for the CrN/MgO interface.

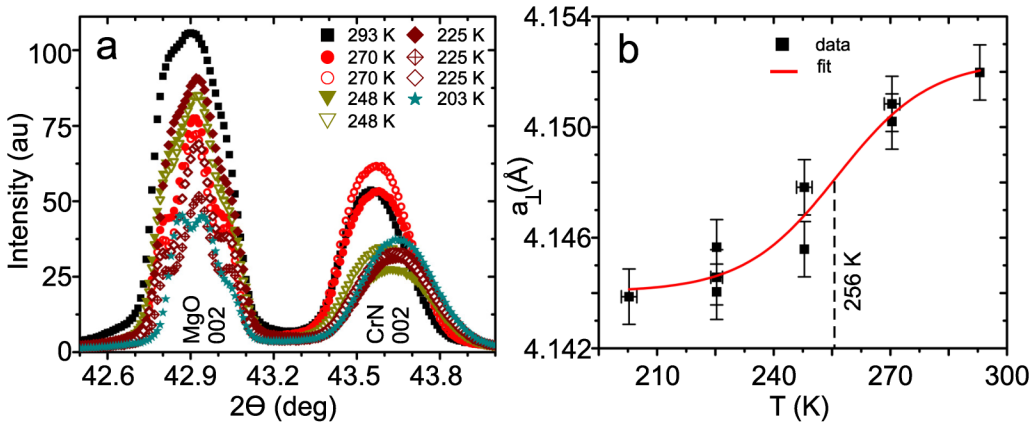

FIG. 4. (a) XRD spectra of 002 peak of MgO and CrN in a range of temperature from 293 to 203 K are shown. (b) CrN thin film goes through a structural phase transition at 256 K.

TABLE I. Film temperature T vs CrN out-of-plane lattice constant.

T (K)	293.0	270.4	270.4	247.9	247.9	225.3	225.3	225.3	202.7
$a_{\perp}$ (Å)	4.152	4.151	4.150	4.148	4.146	4.145	4.146	4.144	4.144

CrN layer is continuous with no cracks in the entire range scanned by the TEM. The difference in the charge densities of CrN and MgO layers produces color contrast, and the CrN layer appears brighter compared to the MgO layer. The thickness of film S73 is 150 nm and of film S45 is 670 nm; however, there is no noticeable difference in the magneto-structural transition temperature of CrN in this thickness range.[14]

An atomically resolved bright-field image of CrN and MgO taken along $[100]_{CrN}$ is shown in Fig. 3(b). Due to the lattice 1.45% of mismatch between CrN and MgO, the first few CrN monolayers at the CrN/MgO interface are expected to have *in-plane* tensile strain. Using Van der Mervwe model[38] for the layer by layer growth, the critical thickness for the CrN layer on MgO substrates is about one monolayer, so the dislocations such as edge dislocation may exist in the film, but have not been observed with the TEM in the scanned area. The *in-plane* strain will reduce with more growth, which can be observed by carefully counting the number of atomic rows at the top and bottom side of Fig. 3(b). For more quantitative analyses, the *in-plane* and *out-of-plane* interplanar spacing are plotted vs atomic rows from the interface in 3(c) and 3(d), respectively. Boltzmann fits on both of the data sets show that the interface is at the 23rd row. Both data sets have been calibrated with the measured MgO lattice constant of 4.213 Å. The Boltzmann equation used for the fit is

$$f = c_{MgO} + [c_{CrN} - c_{MgO}]/[1 + \exp((x - x_0)/dx)],$$

where c_{CrN} and c_{MgO} represent the interplanar spacings of CrN and MgO, x_0 represents position of the interfacial layer, and dx is the slope parameter of the curve. (Note: This slope parameter dx does not correspond to the actual slope of the curve at the inflection point.[39]) Fit parameters for the *in-plane* data set are $c_{MgO} = 2.107 \pm 0.002$ Å, $c_{CrN} = 2.069 \pm 0.002$ Å and $x_0 = 22.79 \pm 0.37$ layer. The CrN interplanar spacing corresponds to an *in-plane* lattice constant ($2\times c_{CrN}$) of 4.139 ± 0.004 Å, which matches with the lattice constant determined by XRD within the margin of error. On the *out-of-plane* data set, the fit is applied with the following parameters $c_{MgO} = 2.107 \pm 0.046$ Å, $c_{CrN} = 2.053 \pm 0.030$ Å and $x_0 = 22.80 \pm 0.40$ layer. The CrN interplanar spacing corresponds to an *out-of-plane* lattice constant of 4.106 ± 0.06 Å. The *out-of-plane* lattice constant of CrN is smaller than the *in-plane* lattice constant due to the *in-plane* tensile strain. From CrN lattice parameters, its Poisson's ratio [ν = (in-plane strain)/(out-of-plane strain)] is determined to be 0.283 ± 0.003, which is in agreement with 0.258 (Ref. 40) and 0.28 (41).

Figure 3(e) shows a zoomed-in view of the CrN(100)/MgO (100) interface, and Fig. 3(f) shows the corresponding model. The CrN lattice is epitaxial with the MgO lattice and Cr is bonded with O of the MgO at the interface as determined by the calculations in this paper. The Cr, N, Mg, and O atoms are represented by blue (large ball in CrN), green (small ball in CrN), red (large ball in MgO), and gray (small ball in MgO) colored balls and labeled in the figure. Both CrN and MgO have a rock salt crystal structure, a square unit cell of the (100) plane of the same size as the model is overlaid on the STEM image. This STEM measurement is consistent with the XRD results and reveals that the epitaxial relationship between CrN and MgO is $[100]_{CrN} \parallel [100]_{MgO}$ and $[001]_{CrN} \parallel [001]_{MgO}$.

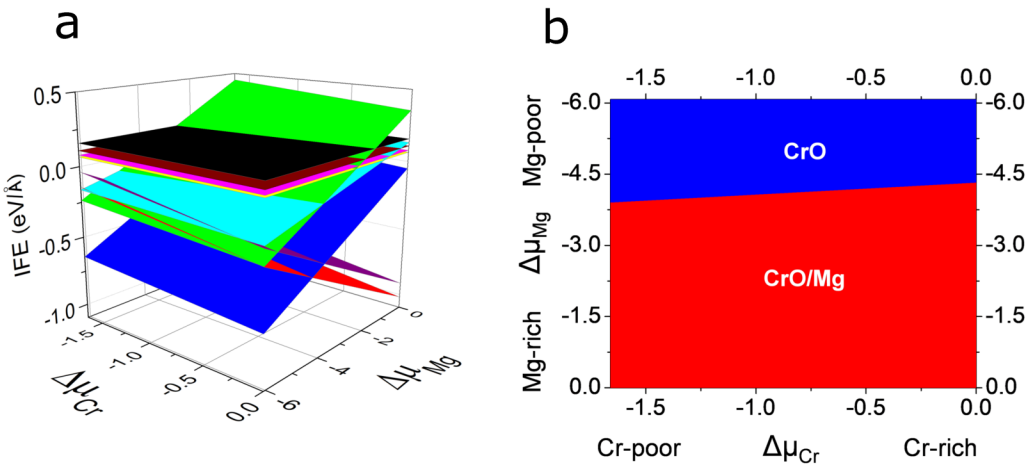

FIG. 5. (a) Interface formation energy formalism in their 3D representation. Each plane represents a different interface, and the reference is the ideal MgO(001) surface (black plane, IFE ~0.2 eV/Å). (b) Phase diagram of the CrN/MgO system. The CrO/Mg model is stable in the red colored region (corresponds to Mg-rich region), and the CrO model is stable in the blue colored region (corresponds to Mg-poor region)

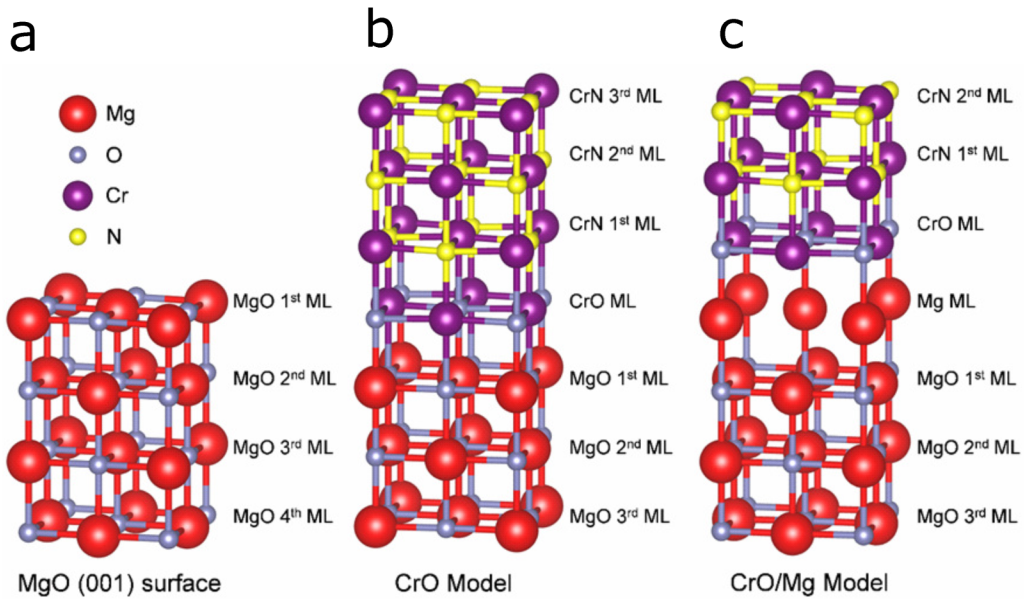

FIG. 6. Structural models for (a) MgO(001) surface, (b) CrO interface, and (c) CrO/Mg interface.

The structural phase transition in CrN thin films is studied by VT-XRD experiments. Sample S45 has been cooled down by flowing nitrogen vapor over the sample from 293 to 203 K and then warmed up by controlling the vapor flow. X-ray diffraction spectra of the sample have been continuously recorded during both the cooling and warming cycle. Figure 4(a) shows that during cooling, the 002 peaks of MgO and CrN shift to the right, and during warming these peaks move to the left representing contraction and expansion of the lattice constants. Since this experiment was not done under vacuum, the difference in intensities is likely due to the ice formation on the surface. The MgO lattice constant contracts linearly for the temperature range of this experiment.[42] As a result, the temperature of the samples is readily determined using MgO data from our experiment and thermal expansion coefficient (α_{MgO}) of $9.84 \times 10^{-6}\,K^{-1}$ (Refs. 43 and 44) in equation $T(K) = 293\,K + \frac{\triangle a}{a_o\,\alpha_{MgO}}$. However, the CrN peak position is found to not shift in a completely linear fashion over the range around the expected phase transition. This trend is observed in the CrN out-of-plane lattice constant ($a_\perp$) vs temperature data presented in Table I and in Fig. 4(b), where $a_\perp$ is plotted vs temperature. A fit to the data is obtained by using the Boltzmann equation,

$$a_\perp(T) = 4.152\,\text{Å} - 0.008\,\text{Å}/[1 + \exp((T - T_N)/\triangle T)],$$

which gives a transition temperature of 256 ± 6 K, which is lower than what we have reported for the CrN thin films studied by variable temperature reflection high energy electron diffraction and variable temperature neutron diffraction experiments.[14] There are two possible reasons for the lower transition temperature observation: first, in this experiment, the film temperature is determined from the linear thermal expansion of MgO; and second, the temperature equilibration time per step was not long enough. Nevertheless, the nonlinear change in the out-of-plane lattice parameter is very clear from the plot shown in Fig. 4(b). On the other hand, assuming linear thermal expansion for the CrN, its thermal expansion coefficient (α_{CrN}) becomes $2.9 \times 10^{-5}\,K^{-1}$, which is 3–4× larger than reported values $0.75–1.06 \times 10^{-5}\,K^{-1}$.[18,45–47] Similar transition in the c axis has been reported by Zieschang *et al.*[48] for CrN nanoparticles.

The CrN/MgO interface model is constructed considering experimental measurements. According to the experiment, CrN and MgO show the epitaxial relationship $[100]_{CrN} \parallel [100]_{MgO}$ and $[001]_{CrN} \parallel [001]_{MgO}$. Both CrN and MgO crystallize in the rock salt crystal structure, with a calculated lattice parameter for MgO of 4.21 Åand a Mg–O bond distance of 2.10 Åand a CrN lattice parameter of 4.14 Åand a Cr–N bond length of 2.07 Å. The calculated lattice mismatch is 1.58%, which is in agreement with experimental measurements.

To investigate the thermodynamic stability of the CrN/MgO (001) interface, various interface models with different types of atoms and with different number densities have been studied. Therefore, we have to use the Interface Formation Energy (IFE) formalism following Ref. 49. In our case, we can define the energy of the CrN/MgO slab as follows:

$$\Lambda_{MgO/CrN} = \frac{E^{Slab}_{CrN/MgO} - E^{Slab}_{CrN} - E^{Slab}_{MgO}}{A} + \Omega_{CrN} + \Omega_{MgO},$$

where $E^{Slab}_{CrN/MgO}$, E^{Slab}_{CrN}, and E^{Slab}_{MgO} are the total energies of the CrN/MgO system, isolated CrN slab, and isolated MgO slab,

TABLE II. Interlayer distances and magnetic moments of different layers close to the interface for the CrO and CrO/Mg models.

Interlayer distance (Å)		Layer	Cr magnetic moment (μ_B)
CrO model			
d_{1-2}	2.07	1	±2.81
d_{2-3}	2.07	2	±2.84
d_{3-4}	2.07	3	±2.88
d_{4-5}	2.07	4	±3.44
d_{5-6}	2.04	5	—
d_{6-7}	2.04	6	—
CrO/Mg model			
d_{1-2}	2.05	1	±2.84
d_{2-3}	2.06	2	±2.85
d_{3-4}	2.06	3	±3.52
d_{4-5}	2.06	4	—
d_{5-6}	2.06	5	—
d_{6-7}	2.05	6	—

respectively; A is the area of the interface. Ω_{CrN} and Ω_{MgO} are defined as

$$\Omega_{CrN} = \frac{1}{2A}\left[E^{Slab}_{CrN} - \frac{1}{2}(n_{Cr}+n_N)\mu^{Bulk}_{CrN} - \frac{1}{2}(n_{Cr}-n_N)(\mu_{Cr}-\mu_N)\right],$$

$$\Omega_{MgO} = \frac{1}{2A}\left[E^{Slab}_{MgO} - \frac{1}{2}(n_{Mg}+n_O)\mu^{Bulk}_{MgO} - \frac{1}{2}(n_{Mg}-n_O)(\mu_{Mg}-\mu_O)\right],$$

where n_i and μ_i are the number of atoms and the chemical potential of the ith species.

A 3D plot in Fig. 5(a) shows IFE vs chemical potentials of Cr and Mg, where each plane represents a different interface model. For CrN, the chemical potential has been varied from Cr-rich conditions ($\mu_{Cr} = \mu^{bulk}_{Cr}$) to Cr-poor conditions ($\mu_{Cr} = \mu^{bulk}_{Cr}$-$\mu^{mol}_N$). For MgO, the chemical potential has been changed from Mg-rich conditions ($\mu_{Mg} = \mu^{bulk}_{Mg}$) to Mg-poor conditions ($\mu_{Mg} = \mu^{bulk}_{Mg}$-$\mu^{mol}_O$). Our reference is the ideal MgO(001) surface (black plane). According to the formalism, the most stable interface has the lowest IFE value. Figure 5(a) shows that the two different interfaces, namely, CrO (blue plane) and CrO/Mg (red plane) are stable, which have been projected to the 2D phase diagram shown in Fig. 5(b). For the entire Cr chemical potential from 0 to −1.66 eV and from Mg-poor to Mg-intermediate conditions (from −6.07 to ∼ −4 eV), the interface is mediated by a monolayer of CrO between the CrN and MgO layers. Oxygen has been acquired during growth by substitution of Mg atoms in the first layer by Cr atoms. At Mg-rich and Mg-intermediate conditions (from 0 to ∼ 4 eV) and for the entire range of $\triangle\mu_{Cr}$, the most favorable model is the CrO/Mg model. In this case, the O atoms of the first layer migrate upwards to be placed on top of the Mg atoms and form a monolayer of CrO. The result is an interface formed by a layer of CrO and a layer of Mg below.

The crystal structures of the ideal MgO(001) surface [Fig. 6(a)], CrO [Fig. 6(b)] and CrO/Mg [Fig. 6(c)] interface models are shown in Fig. 6. Two types of Mg–O bonds can be distinguished: bonds parallel (*in-plane*) and perpendicular (*out-of-plane*) to the surface. Parallel Mg–O bonds have the same values as those in bulk, but perpendicular Mg–O bonds suffer from an expansion or a contraction depending on the type of atom exposed at the surface. If the most exposed atom is oxygen, the bond distance increases to 2.12 Å, but if the most exposed atom is Mg, the bond contracts to 2.09 Å. At the interface, in both stable models, parallel Cr–N bonds suffer from an expansion in comparison with bulk from 2.07 to 2.10 Å. Also, in comparison with the MgO(001) surface, the interplanar distance between MgO layers close to the interface is contracted. For the CrO model, the CrO layer shows an interplanar distance with the upper CrN and lower MgO layer of 2.07 Å. In the case of the CrO/Mg model, the interplanar distance between the CrO and Mg layers is 2.06 Å, the distance between CrO and CrN is 2.06 Å, and the interlayer distance between the Mg ML and the lower MgO is 2.06 Å. Table II summarizes the interlayer distance of the different models. Experimentally, the CrN epitaxial growth is carried out under N-rich conditions. According to the calculated phase diagram, under N-rich (Cr-poor) conditions, both interfaces could appear at different ranges of the Mg chemical potential. Both models have similar interlayer distances and structural characteristics, so both CrO and CrO/Mg could grow as the first layer at the interface.

The CrN (001) surface is antiferromagnetic. The aFM configuration is formed by alternating FM layers along the [100] direction in concordance with previous reports.[14,22,31] Therefore, each monolayer of CrN perpendicular to the growth direction is aFM. The Cr magnetic moments of the most exposed atoms are $\pm 2.84\ \mu_B$, while the inner layers have magnetic moments of $\pm 2.78\ \mu_B$, the increase in the magnetic moment of the most exposed layer could be attributed to the low coordination of the most exposed atoms. When CrN is epitaxially grown on MgO(001) substrates, our calculations demonstrate that the magnetic configuration does not change at the interface. However, we observed that the Cr magnetic moments increase close to them. In both models, the CrO layer exhibits magnetic moments larger than $\pm 3.44\ \mu_B$. The neighboring layers of CrN show magnetic moments of $\sim \pm 2.9\ \mu_B$. Also, the inner CrN layers have magnetic moments close to the bulk value, which is consistent with the reported observation.[50] The increase in the Cr magnetic moments is attributed to the interaction between Cr and O atoms. Table II summarizes the magnetic moments of both stable models.

IV. CONCLUSIONS

High quality CrN thin films on MgO(001) substrates prepared by MBE. A temperature dependent structural phase transition in the films is studied using VT-XRD. The CrN film grows epitaxially on MgO substrates such that $[100]_{CrN} \parallel [100]_{MgO}$, $[110]_{CrN} \parallel [110]_{MgO}$, and $[001]_{CrN} \parallel [001]_{MgO}$. VT-XRD experiments indicate a first-order structural phase transition in the CrN films. The density functional theory based calculations show that there are two stable interfaces form betwen CrN and MgO: the CrO model, where Mg atoms in the top layer have been substituted by Cr atoms and, in the other model, O moves up to form CrO layer and leave a pure Mg monolayer. With respect to the magnetic properties,

calculations show that the aFM behavior observed on the CrN(001) surfaces remains at the interface. However, an increase in the Cr magnetic moments close to the interface has been noticed due to the interactions with the oxygen.

ACKNOWLEDGMENTS

Research has been supported by IRC for Renewable Energy and Power Systems at King Fahd University of Petroleum and Minerals, Dhahran, Saudi Arabia under Grant No. INRE2216 (data analysis and manuscript preparation) and by the U.S. Department of Energy, Office of Basic Energy Sciences, Division of Materials Sciences and Engineering under Award No. DE-FG02-06ER46317 (MBE growth, RHEED, and XRD studies).

R.P.P. and N.T. thank DGAPA-UNAM under Project Nos. IN101523, IN105722, and IA100624 and CONACyT under Grant No. A1-S-9070 for partial financial support. Calculations were performed in the DGCTIC-UNAM Supercomputing Center, Project Nos. LANCAD-UNAM-DGTIC-051, LANCAD-UNAM-DGTIC-150, and LANCAD-UNAM-DGTIC-422. We thank E. Murillo and Aldo Rodriguez-Guerrero for technical support and useful discussions.

AUTHOR DECLARATIONS

Conflict of Interest

The authors have no conflicts to disclose.

Author Contributions

Khan Alam: Conceptualization (equal); Data curation (equal); Formal analysis (equal); Investigation (equal); Methodology (equal); Visualization (equal); Writing – original draft (equal); Writing – review & editing (equal). Rodrigo **Ponce-Pérez:** Formal analysis (equal); Writing – review & editing (equal). **Kai Sun:** Investigation (equal); Writing – review & editing (equal). **Andrew Foley:** Investigation (equal); Writing – review & editing (equal). **Noboru Takeuchi:** Investigation (equal); Writing – review & editing (equal). **Arthur R. Smith:** Conceptualization (equal); Data curation (equal); Funding acquisition (equal); Investigation (equal); Project administration (equal); Resources (equal); Supervision (equal); Writing – original draft (equal); Writing – review & editing (equal).

DATA AVAILABILITY

The data that support the findings of this study are available from the corresponding author upon reasonable request.

REFERENCES

[1]B. Wei, H. Liang, D. Zhang, Z. Wu, Z. Qi, and Z. Wang, J. Mater. Chem. A **5**, 2844 (2017).
[2]E. Haye *et al.*, Electrochim. Acta **324**, 134890 (2019).
[3]T. Yotsuya, Y. Kakehi, and T. Ishida, Cryogenics **51**, 546 (2011).
[4]I. Batko, M. Batkova, and F. Lofaj, Acta Phys. Pol. A **126**, 415 (2014).
[5]K. Alam, K.-Y. Meng, R. Ponce-Pérez, G. H. Cocoletzi, N. Takeuchi, A. Foley, F. Yang, and A. R. Smith, J. Phys. D: Appl. Phys. **53**, 125001 (2020).
[6]B. Biswas, S. Chakraborty, O. Chowdhury, D. Rao, A. I. K. Pillai, V. Bhatia, M. Garbrecht, J. P. Feser, and B. Saha, Phys. Rev. Mater. **5**, 114605 (2021).
[7]M. Yuan, X. Wan, Q. Meng, X. Lu, L. Sun, W. Wang, P. Jiang, and X. Bao, Mater. Today Phys. **19**, 100420 (2021).
[8]Y. Song, Y.-F. Zhang, J. Pan, and S. Du, Chin. Phys. B **30**, 047105 (2021).
[9]K. Nie, X. Wang, and W. Mi, Phys. Chem. Chem. Phys. **21**, 6984 (2019).
[10]L. Corliss, N. Elliott, and J. Hastings, Phys. Rev. **117**, 929 (1960).
[11]A. Filippetti and N. A. Hill, Phys. Rev. Lett. **85**, 5166 (2000).
[12]P. Bhobe *et al.*, Phys. Rev. Lett. **104**, 236404 (2010).
[13]A. Mrozińska, J. Przystawa, and J. Sòlyom, Phys. Rev. B **19**, 331 (1979).
[14]K. Alam *et al.*, Phys. Rev. B **96**, 104433 (2017).
[15]A. Garzon-Fontecha, H. Castillo, E. Restrepo-Parra, and W. De La Cruz, Surf. Coat. Technol. **334**, 98 (2018).
[16]C. Constantin, M. B. Haider, D. Ingram, and A. R. Smith, Appl. Phys. Lett. **85**, 6371 (2004).
[17]K. Inumaru, K. Koyama, N. Imo-Oka, and S. Yamanaka, Phys. Rev. B **75**, 054416 (2007).
[18]X. Zhang, J. Chawla, R. Deng, and D. Gall, Phys. Rev. B **84**, 073101 (2011).
[19]T. Rojas and S. E. Ulloa, Phys. Rev. B **96**, 125203 (2017).
[20]K. Alam, R. Ponce-Pérez, K. Sun, A. Foley, N. Takeuchi, and A. R. Smith, J. Vac. Sci. Technol. A **39**, 063209 (2021).
[21]A. Ney, R. Rajaram, S. Parkin, T. Kammermeier, and S. Dhar, Appl. Phys. Lett. **89**, 112504 (2006).
[22]R. Ponce-Pérez, K. Alam, G. H. Cocoletzi, N. Takeuchi, and A. R. Smith, Appl. Surf. Sci. **454**, 350 (2018).
[23]K. Alam, M. B. Haider, M. F. Al-Kuhaili, K. A. Ziq, and B. U. Haq, Ceram. Int. **48**, 17352 (2022).
[24]W. Lin, A. Foley, K. Alam, K. Wang, Y. Liu, T. Chen, J. Pak, and A. R. Smith, Rev. Sci. Instrum. **85**, 043702 (2014).
[25]K. Alam, A. Foley, and A. R. Smith, Nano Lett. **15**, 2079 (2015).
[26]G. Kresse and J. Hafner, Phys. Rev. B **47**, 558 (1993).
[27]D. M. Ceperley and B. J. Alder, Phys. Rev. Lett. **45**, 566 (1980).
[28]P. E. Blöchl, Phys. Rev. B **50**, 17953 (1994).
[29]G. Kresse and D. Joubert, Phys. Rev. B **59**, 1758 (1999).
[30]S. L. Dudarev, G. A. Botton, S. Y. Savrasov, C. Humphreys, and A. P. Sutton, Phys. Rev. B **57**, 1505 (1998).
[31]R. Ponce-Pérez, G. H. Cocoletzi, and N. Takeuchi, Appl. Surf. Sci. **573**, 151451 (2022).
[32]F. Gao, J. Hu, C. Yang, Y. Zheng, H. Qin, L. Sun, X. Kong, and M. Jiang, Solid State Commun. **149**, 855 (2009).
[33]H. J. Monkhorst and J. D. Pack, Phys. Rev. B **13**, 5188 (1976).
[34]See the supplementary material online for the simulated XRD data of MgO and CrN and their comparison with the experimental data.
[35]O. Köksal and R. Pentcheva, Phys. Rev. B **103**, 045135 (2021).
[36]M. Benkahoul, P. Robin, S. Gujrathi, L. Martinu, and J. Klemberg-Sapieha, Surf. Coat. Technol. **202**, 3975 (2008).
[37]D. Gall, C.-S. Shin, T. Spila, M. Odén, M. J. H. Senna, J. E. Greene, and I. Petrov, J. Appl. Phys. **91**, 3589 (2002).
[38]A. Kumar and A. Subramaniam, Appl. Surf. Sci. **275**, 60 (2013).
[39]K. Heusser, R. Heusser, J. Jordan, V. Urechie, A. Diedrich, and J. Tank, Front. Neurosci. **15**, 697582 (2021).
[40]M. Yan and H. Chen, Comput. Mater. Sci. **88**, 81 (2014).
[41]L. Cunha, M. Andritschky, K. Pischow, and Z. Wang, Thin Solid Films **355**, 465 (1999).
[42]D. C. Harris *et al.*, J. Am. Ceram. Soc. **96**, 3828 (2013).
[43]O. Madelung, *Semiconductors: Data Handbook*, 3rd ed. (Springer, New York, 2004).
[44]L. Liu, K. Morita, T. S. Suzuki, and B.-N. Kim, J. Eur. Ceram. Soc. **41**, 2096 (2021).
[45]G. Janssen, F. Tichelaar, and C. Visser, J. Appl. Phys. **100**, 093512 (2006).
[46]L. Zhou, F. Körmann, D. Holec, M. Bartosik, B. Grabowski, J. Neugebauer, and P. H. Mayrhofer, Phys. Rev. B **90**, 184102 (2014).
[47]R. Daniel, D. Holec, M. Bartosik, J. Keckes, and C. Mitterer, Acta Mater. **59**, 6631 (2011).
[48]A.-M. Zieschang, J. D. Bocarsly, M. Dürrschnabel, H.-J. Kleebe, R. Seshadri, and B. Albert, Chem. Mater. **30**, 1610 (2018).
[49]J. Guerrero-Sánchez and N. Takeuchi, Comput. Mater. Sci. **144**, 294 (2018).
[50]B. U. Haq, K. Alam, M. B. Haider, A. M. Alsharari, S. Ullah, and S.-H. Kim, Physica E **150**, 115697 (2023).